

Exploring ultra-high-intensity wakefields in carbon nanotube arrays: an effective plasma-density approach

A. Bonatto*

*Graduate Program in Information Technology and Healthcare Management, and the Beam Physics Group,
Federal University of Health Sciences of Porto Alegre, Porto Alegre, RS, 90050-170, Brazil*

G. Xia and O. Apsimon

*Department of Physics and Astronomy, The University of Manchester, Manchester, M13 9PL, United Kingdom
and The Cockcroft Institute, Sci-Tech Daresbury, Warrington, WA4 4AD, United Kingdom*

C. Bontoiu, E. Kukstas, V. Rodin, M. Yadav, and C. P. Welsch

*Department of Physics, The University of Liverpool, Liverpool, L69 3BX, United Kingdom
and The Cockcroft Institute, Sci-Tech Daresbury, Warrington, WA4 4AD, United Kingdom*

J. Resta-López†

ICMUV, Instituto de Ciencia de los Materiales, Universidad de Valencia, 46071 Valencia, Spain

(Dated: November 15, 2022)

Charged particle acceleration using solid-state nanostructures has attracted attention in recent years as a method of achieving ultra-high-gradient acceleration in the TV/m domain. More concretely, metallic hollow nanostructures could be suitable for particle acceleration through the excitation of wakefields by a laser or a high-intensity charged particle beam in a high-density solid-state plasma. For instance, due to their special channelling properties as well as optoelectronic and thermo-mechanical properties, carbon nanotubes could be an excellent medium for this purpose. This article investigates the feasibility of generating ultra-high gradient acceleration using carbon nanotube arrays, modelled as solid-state plasmas in conventional particle-in-cell simulations performed in a two-dimensional axisymmetric (*quasi*-3D) geometry. The generation of beam-driven plasma wakefields depending on different parameters of the solid structure is discussed in detail. Furthermore, by adopting an effective plasma-density approach, existing analytical expressions, originally derived for homogeneous plasmas, can be used to describe wakefields driven in periodic non-uniform plasmas.

I. INTRODUCTION

High-energy particle accelerators are predominantly based on radiofrequency (RF) technology. However, standard RF technology is limited to gradients of the order of 100 MV/m due to surface breakdown [1]. Thus, larger and more expensive accelerator facilities are necessary in order to obtain higher energy particle beams. Therefore, R&D into novel accelerator techniques is important to overcome the present acceleration limitations towards more compact and cost-effective solutions. Several alternative paths towards high-gradient acceleration are currently being investigated, e.g. techniques using dielectric microstructures [2–4] or plasmas as accelerating media. For instance, plasma wakefield acceleration (PWFA) methods based on gaseous plasma have been shown to produce gradients of up to approximately 100 GV/m [5–8]. For typical gaseous plasmas used as acceleration media, the maximum achievable accelerating gradient is limited by the so-called plasma wave-breaking limit, which depends on the plasma density. In the linear regime, this limit, known as the cold non-relativistic

wave breaking field [9], is given by

$$E_0[\text{V/m}] = m_e c \omega_p / e \simeq 96 \sqrt{n_0 [\text{cm}^{-3}]}, \quad (1)$$

where m_e and e are the electron mass and charge, respectively, c is the speed of light in vacuum, $\omega_p = [n_0 e^2 / (\epsilon_0 m_e)]^{1/2}$ is the plasma frequency, n_0 is the plasma density and ϵ_0 is the vacuum permittivity. To surpass present PWFA limits, solid-based acceleration media, such as crystals or nanostructures could offer a solution. The density of charge carriers (conduction electrons) in solids is four or five orders of magnitude higher than those in a gaseous plasma, thus offering the possibility to obtain ultra-high gradients on the order of $E_0 \sim 1\text{--}10$ TV/m, if the same linear theory is assumed.

Solid-state wakefield acceleration using crystals was proposed in the 1980s and 1990s by T. Tajima and others [10, 11] as an alternative particle acceleration technique to sustain TV/m acceleration gradients. In the original Tajima's conceptual scheme, a metallic crystal is excited by a laser (laser driven), generating a longitudinal electric wakefield which can be used as an accelerating structure. Then, if a witness beam of charged particles is injected into the crystal with an optimal injection angle for channelling and with the right phase with respect to the wakefield, the channelled particles can ex-

* abonatto@ufcspa.edu.br

† javier2.resta@uv.es

perience acceleration. To reach accelerating gradients on the order of 1–10 TV/m, crystals must be excited by ultrashort X-ray laser pulses within a power range of TW–PW, which makes the practical realisation of the concept very challenging. It has only recently become a realistic possibility since the invention of the single-cycled optical laser compression technique by G. Mourou et al. [12]. Although simulation studies of X-ray wakefield acceleration have been performed [13], it has not been experimentally demonstrated yet. Alternatively, channelled particles in crystals can also be accelerated by means of electric wakefields excited by ultrashort, relativistic electron bunches (beam driven). In this case the energy losses of a driving bunch can be transformed into the acceleration energy of a witness bunch.

If natural crystals (e.g. silicon) are used for the solid-state wakefield acceleration, the beam intensity acceptance is significantly limited by the angstrom-size channels. In addition, such small size channels increase the dechannelling rate and make channels physically vulnerable to high energy interactions, thus increasing the damage probability by high power beams.

Over the past decade there have been great advances in nanofabrication techniques [14–16] that could offer an excellent way to overcome many of the limitations of natural crystals. Metallic nanostructures and metamaterials [17, 18] may offer suitable ultra-dense plasma media for wakefield acceleration or charged particle beam manipulation, i.e. channelling, bending, wiggling, etc. This also includes the possibility of investigating new paths towards ultra-compact X-ray sources [17].

In this context, the use of nanotube structures for generating ultra-high gradients is attracting attention [19–21]. For instance, carbon nanotube (CNT) based structures can help to relax the constraints to more realistic regimes with respect to natural crystals. CNTs present the following advantages with respect to natural crystals: (i) larger degree of dimensional flexibility and thermo-mechanical strength; (ii) transverse acceptances of the order of up to 100 nm, i.e. three orders of magnitude higher than a typical silicon channel; (iii) lower dechannelling rate; (iv) less disruptive effects such as filamentation and collisions. Therefore, CNTs are a robust candidate for solid-state wakefield acceleration.

Wakefields in crystals or nanostructures can be induced by means of the excitation of high-frequency collective motion of conduction electrons through the crystalline ionic lattice. This collective oscillation of conduction electrons in metals, excited by external electromagnetic fields is commonly referred to as plasmon [22]. For instance, the excitation of surface plasmonic modes [23–26], driven either by charged particle beam [27–30] or by laser [13, 31], could be used as a collective mechanism to generate high acceleration gradients in metallic nanotubes. To be effective, the driver dimensions should match the spatial (\sim nm) and time (sub-femtoseconds) scales of the excited plasmonic oscillations. Wakefield-driving sources working on these scales are now experimentally realiz-

able. For instance, attosecond X-ray lasers are possible thanks to the pulse compression technique invented by Donna Strickland and Gerard Mourou [32]. In the case of beam-driven wakefields, the experimental facility FACET-II at SLAC [33] will allow the access to "quasi-solid" and ultra-short electron beams, with densities up to $\sim 10^{30} \text{ m}^{-3}$ and sub-micrometer bunch length scale. Recent studies have reported that ultra-short and high-density electron beams could lead to a nonlinear plasmonic regime, generating acceleration gradients beyond TV/m in micro- and nano-tubes. This is also known as the *crunch-in* regime [34–36] and could be a potential step towards the realisation of compact PeV colliders [37].

In this article we study the feasibility of generating ultra-high acceleration gradients in nanostructures based on CNTs. In addition, we show that, under proper conditions, by adopting an effective density, existing analytical estimates, originally derived for wakefields driven in homogeneous plasmas in the linear regime, can be used to describe the wakefields excited in such nanostructures. In particular, for multiple target configurations (single hollow plasma channel/CNT, CNT arrays) the amplitude of the longitudinal beam-driven wakefield is evaluated and compared to – and shown to be in agreement with – analytical estimates for the amplitude of longitudinal beam-driven wakefields, obtained by using an effective-density approach, as described along this work. Moreover, existing results [21] for CNT beam-driven wakefields, previously simulated using 2D Cartesian geometry have been revisited with FBPIC [38], using a 2D axisymmetric geometry. Regarding the structure of this work, in Section II the simulation model is described. Section III investigates the case of beam-driven wakefields in single tubes, and the role of key parameters, such as tube wall thickness and aperture, is systematically studied. Section IV focuses on the case of an aligned multichannel structure, representing a CNT array. Highly-ordered nanotube bundles would allow to fabric macroscopic samples with transverse width on the order of centimetres, thus being able to cover all the transverse cross sections for beam waist-sizes on the order of tens and hundreds of micrometres. In this case, where we deal with an inhomogeneous plasma structure, the feasibility of using an effective-density approach is investigated. Finally, some conclusions are drawn in Section V.

II. SIMULATION MODEL

Hollow plasma channels (HPC), consisting of cylindrical shells populated by heavy ions, with mass $m_i = 12 m_p$, where m_p is the proton mass, and free, pre-ionised electrons, are adopted here as a first-order approximation to describe a CNT, or a larger structure made of CNT bundles, as shown in Fig. 1. Although this collisionless fluid-model does not take into account the solid state properties emerging from the ionic lattice, such as, for example, the presence of polaritons, previous stud-

ies have shown that the wakefield formation and electron acceleration processes in crystalline structures are only slightly affected by the ionic lattice force [39]. Therefore, neglecting the ionic effects at a first approximation might be justified, and – if this is the case – conventional particle-in-cell (PIC) codes might be an useful tool to investigate ultra high-gradient acceleration, as well as plasmon modelling in solids [13, 35, 40]. As it has been already shown [40], the PIC method can be very suitable to model solid-state based plasmons, since it self-consistently solves the fields and the motion of a large assembly of charged particles for the required time (\sim sub-fs) and spatial (\sim nm) scales.

Due to the high computational cost of 3D PIC simulations, the 2D Cartesian geometry is often adopted. In such geometry, CNT walls are modelled as flat plasma sheets, with finite thickness and length, and infinite width. However, this geometry is known to affect the spatial derivatives of the fields [41] if applied to describe a non-slab-like system. Given the close-to-cylindrical symmetry of the physical system under consideration, a PIC code with a spectral solver can provide an accurate 3D description of the system, at a computational cost similar to the cost of performing 2D Cartesian PIC simulations [42].

In this work, the Fourier-Bessel Particle-in-Cell (FBPIC) code [38] is adopted to perform the simulations using the cylindrical CNT hollow plasma channel model. Although particles in FBPIC have 3D Cartesian coordinates, its solver uses a set of 2D radial grids, each of them representing an azimuthal mode m ($m = 0, 1, \dots$). While the first mode ($m = 0$) describes axisymmetric fields, higher-order modes can be added to model departures from the cylindrical symmetry. For example, a linearly polarised laser can be computed by adding the mode $m = 1$. An interesting feature of the spectral solver implementation in FBPIC is the mitigation of spurious numerical dispersion, including the zero-order numerical Cherenkov effect [43].

Compact high-energy electron beams are often reported in literature with dimensions ranging from a fraction to a few micrometers [33, 44]. Therefore, in this work, beams with near- μm RMS sizes are used as drivers to excite the intense wakefields in hollow plasma channels, which are under investigation in this section. The beam driver is assumed to have a bi-Gaussian density profile,

$$n_b(\xi, r)/n_0 = (n_b/n_0) e^{-\xi^2/(2\sigma_\xi^2)} e^{-r^2/(2\sigma_r^2)}, \quad (2)$$

where $\xi \equiv z - ct$ is the beam co-moving coordinate, c is the speed of light in vacuum, $n_b \equiv (Q/e)/[(2\pi)^{3/2}\sigma_\xi\sigma_r^2]$ is the peak beam-density, n_0 is the plasma electron density, Q is the beam charge and σ_ξ , σ_r are the beam longitudinal and radial RMS sizes, respectively. The beam has initial kinetic energy E_{k0} , and energy spread $\delta E_{k0}/E_{k0} = 1\%$. In addition, E_{k0} is chosen to ensure

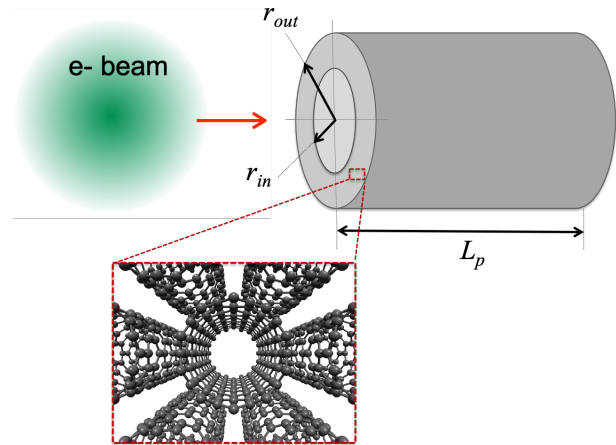


FIG. 1: Top: Schematic model for beam-driven wakefield simulation using a hollow cylinder of solid-state plasma confined in a wall of thickness $r_{out} - r_{in}$ and length L_p . Bottom: In this model the cylinder wall represents a solid made of CNT bundles (not to scale).

that the corresponding relativistic factor γ satisfies the condition $\gamma \gg 1$, in order to increase the beam stiffness.

III. SINGLE TUBE IN 2D AXISYMMETRIC GEOMETRY

As a first approach, a single HPC is adopted as the medium for the beam-driven wakefield excitation. Figure 1 depicts a schematic of the system, in which an electron beam (driving source) is injected into a hollow plasma channel. The plasma is confined in the channel wall, assumed to be made up of CNT bundles. In principle, modern techniques allow for the fabrication of macroscopic materials based on aligned single and multi-wall CNT bundles or CNT forest films [45–47]. In this nanostructured materials, the density profile of the plasma can be controlled by the packaging configuration of the CNTs. By varying parameters from this structure, such as internal radius, wall thickness, and plasma density, it is possible to verify how the wakefield intensity is affected. In order to accommodate a near- μm beam, the hollow plasma channel also has a micrometer-scale.

Typical electron densities (n_e) in solid-state plasmas lie within the range of $10^{19} \text{ cm}^{-3} \leq n_e \leq 10^{24} \text{ cm}^{-3}$ [48, 49]. By selecting the lower limit of this range as the initial density n_0 , for both electrons and ions, i.e., $n_e = n_i = n_0 = 10^{19} \text{ cm}^{-3}$, where n_i is the ion density, a plasma wavelength of $\lambda_p = 10.6 \mu\text{m}$ is obtained. From now on, this quantity (λ_p) is adopted as the characteristic length scale to define the HPC and beam dimensions as follows. The HPC has a length $L_p = 10 \lambda_p$, internal radius $r_{in} = 0.1 \lambda_p$, and external radius $r_{out} = 0.5 \lambda_p$. Therefore, the HPC wall thickness is $w = r_{out} - r_{in} = 0.4 \lambda_p$. Regarding

the beam, both the longitudinal and radial RMS sizes are $\sigma_\xi = \sigma_r = 0.1 \lambda_p$. For such dimensions, a charge of $Q = 33$ pC is chosen, providing a normalised peak beam-density of $n_b/n_0 = 1.1$, i.e., right after the transition from an overdense to an underdense propagation in the plasma, in order to ensure that the beam will experience linear focusing forces [50, 51]. The initial beam-energy is $E_{k0} = 1$ GeV, with an energy spread of $\delta E_{k0}/E_{k0} = 1\%$, and the transverse normalised beam emittance is null. Such parameters were chosen to produce a stiff beam, able to drive a stable wakefield along its propagation. Since the amplitude of the wakefield is evaluated and compared in multiple situations along the investigation, this is a relevant matter.

Figure 2 shows PIC simulation results for the aforementioned parameters, taken at a propagation distance of $z = 53 \mu\text{m}$, corresponding to $L_p/2 = 5 \lambda_p$. Despite the betatron motion of individual beam particles, due to its high initial energy, the beam density profile remains mostly unchanged during the propagation. Figure 2(a) depicts the beam (*transparent-blue-green-yellow* color scale) and plasma-electron (*purple* color scale) densities, in units of the initial plasma density n_0 , both being saturated (capped) in order to enhance the visualization of how these densities are mutually affected. At this propagation distance, the beam density has been slightly modulated, being lower within the CNT walls due to the beam-wall interference. Regarding the plasma electrons, after being radially expelled by the beam, they experience a strong restoring force due to the carbon ions (not shown in this figure), which remain mostly undisturbed. As a consequence, these electrons are tightly focused, creating on-axis density spikes 20 to 35 times higher than the initial plasma density n_0 . This behaviour has been described by Sahai *et al.* as the *crunch-in* regime [34–36]. The periodic transverse motion of plasma electrons, caused by the competition between the Coulomb repulsion and the restoring force due to the ions, creates an intense wakefield, which could be used as an accelerating structure for a witness beam. Figure 2(b) shows the accelerating (negative) phase of the longitudinal wakefield $E_z(\xi, r)$ peaking at $|E_z^{max}| \simeq 105$ GV/m. This value is approximately one third of the cold non-relativistic wave breaking field E_0 calculated for the chosen density. The transverse wakefield, $W_\perp(\xi, r) = E_r - cB_\theta$, with E_r the radial component of the electric field and B_θ the azimuthal component of the magnetic field, is shown in Fig. 2(c). While appreciable amplitudes can be seen within the CNT wall for both focusing and defocusing phases of the transverse wakefield, inside the CNT (i.e., for $r < r_{in}$) there are regions in which the transverse wakefield is approximately null. Due to this interesting feature, the use of hollow plasma channels to mitigate beam quality degradation caused by transverse effects is an active field of research [52–57].

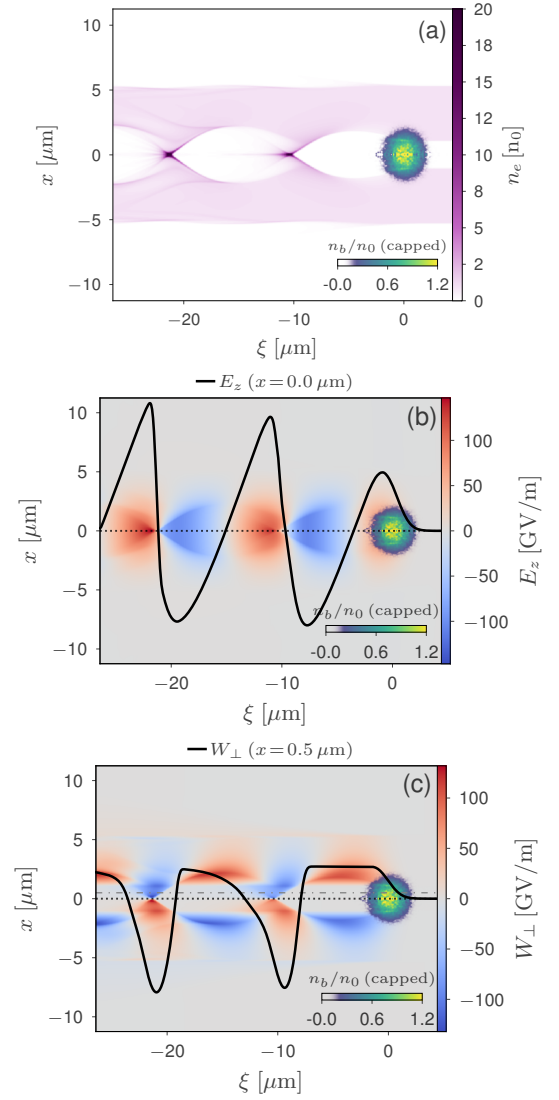


FIG. 2: Bi-Gaussian electron beam ($\sigma_\xi = \sigma_r = 0.1 \lambda_p$) propagating along a hollow plasma channel with $r_{in} = 0.1 \lambda_p$, and $r_{out} = 0.5 \lambda_p$. Panel (a) shows the plasma-electron density (*purple* color scale), and panels (b) and (c) depict the longitudinal and transverse beam-driven wakefields, E_z and W_\perp , respectively, obtained from PIC simulation results (*blue-grey-red* colored areas). The *thick, solid black* lines represent E_z on-axis ($x = 0$), and W_\perp at $x = 0.5 \mu\text{m}$. The beam density (*transparent-blue-green-yellow* color scale) is shown in all panels as well.

A. Tube aperture and wall thickness

Parameter scans might be helpful to determine the optimal system dimensions or aspect ratios to achieve as high amplitude wakefield as possible. In this sense, while maintaining the beam parameters and plasma density fixed, we have investigated the dependence of the longitudinal wakefield on both, tube aperture and wall

thickness. In the first case, the inner tube radius r_{in} has been varied. For instance, Fig. 3, plotted for a fixed wall thickness $w = 0.2 \lambda_p$, illustrates the tube electron density and beam density for the extreme (smallest and largest) investigated values of inner radius r_{in} , for a propagation distance of approximately $z = 70 \mu\text{m}$. While in Fig. 3(a), plotted for $r_{in} = 0.05 \lambda_p < \sigma_r (= 0.1 \lambda_p)$, the beam transversely overlaps the tube wall, in Fig. 3(b), plotted for $r_{in} = 0.50 \lambda_p > \sigma_r$, the tube inner radius is larger than the transverse beam size. The beam density color scale was saturated (capped) at 75% of its maximum value, in order to improve the visualisation of how this quantity is affected by the interference with the tube wall. This saturation has been adopted for all beam density plots in this document. If the beam transversely overlaps the tube inner surface, (Fig. 3(a)) ionised electrons can move from the wall to the centre of the tube and form density bubbles, such as it is observed in a typical blowout regime or a nonlinear plasmonic regime [34–36]. For a large tube aperture with respect to the transverse beam size (Fig. 3(b)), with an initial normalised peak beam-density $n_b/n_0 \sim 1$, the excitation of electrons from the tube wall is much smaller and, in this case, we only expect the excitation of linear surface plasmonic modes.

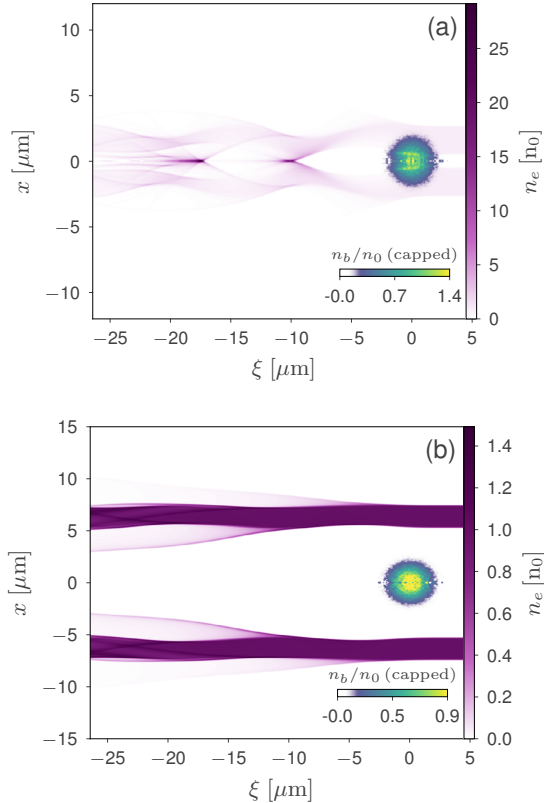


FIG. 3: Tube electron density (purple color scale) and beam density (transparent-blue-green-yellow color scale), capped at 75% of its maximum value ($w = 0.2 \lambda_p$, $z \simeq 70 \mu\text{m}$). (a) $r_{in} = 0.05 \lambda_p$, and (b) $r_{in} = 0.50 \lambda_p$.

Results for the r_{in} scan carried out with the FBPIC code are shown in Fig. 4, in which the longitudinal wakefield amplitude E_z^{max} , taken from the accelerating wake phase – and thus, negative – and normalised by E_0 , plotted as a function of the inner radius r_{in} . A maximum $|E_z^{max}|$ amplitude is obtained at $r_{in} \approx 0.1 \lambda_p$. For $r_{in} > 0.1 \lambda_p$ the longitudinal wakefield amplitude experiences a dramatic decrease, first a parabolic decline for $0.1 \lambda_p < r_{in} < 0.16 \lambda_p$, and a smoother decrease for $r_{in} > 0.16 \lambda_p$. Exactly the same behaviour is observed for two different plasma densities, $n_e = 10^{25} \text{ m}^{-3}$ and $n_e = 10^{26} \text{ m}^{-3}$. It is interesting to observe that the PIC simulation points in Fig. 4 fit well to two q-Gaussian functions:

$$|E_z^{max}|/E_0 \simeq 0.32 e^{-197.8(0.10 - r_{in}/\lambda_p)^2} + 7.80 e^{-0.42(-r_{in}/\lambda_p - 2.85)^2}. \quad (3)$$

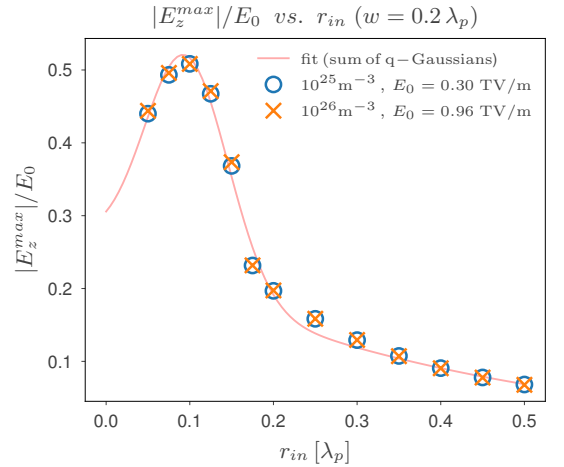


FIG. 4: Normalised maximum accelerating wakefield, $|E_z^{max}|/E_0$, plotted as a function of the internal radius r_{in} in units of λ_p , for a constant wall thickness $w = 0.2 \lambda_p$. Nearly identical PIC results were obtained for $n_e = 10^{25} \text{ m}^{-3}$ (blue circles) and $n_e = 10^{26} \text{ m}^{-3}$ (orange crosses). The obtained data can be fitted by a sum of two q-Gaussians (solid line), written in Eq. (3).

Another key parameter is the wall thickness $w = r_{out} - r_{in}$. Considering a plasma density of $n_e = 10^{25} \text{ m}^{-3}$ and a fixed internal channel radius set as $r_{in} = 0.1 \lambda_p$, Fig. 5 shows the result of the longitudinal amplitude as a function of w . A maximum gradient is obtained at $w \approx 0.22 \lambda_p$. The curve is very non-linear, and it seems to show an asymptotic behaviour for $w > 0.3 \lambda_p$, stabilising the values of the maximum achievable $|E_z^{max}|$ at a value of approximately $0.35 E_0$, with $E_0 = 0.3 \text{ TV/m}$. In this case the simulation results show a good fit to the following function:

$$|E_z^{max}|/E_0 \simeq 0.28 e^{-384.67(0.21 - w/\lambda_p)^2} + 0.11 \ln(w/\lambda_p) + 0.45. \quad (4)$$

Eventually, expressions such as (3) and (4) might allow one to make relatively quick estimates of the longitudinal wakefield amplitude as a function of inner radius and wall thickness, respectively, for these kinds of tubular structures.

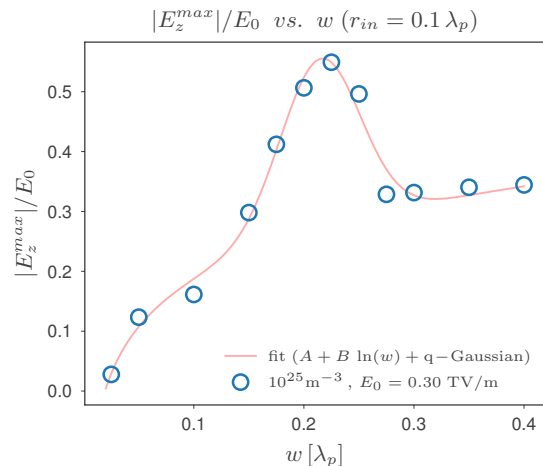


FIG. 5: Maximum accelerating wakefield $|E_z^{max}|/E_0$ vs. wall thickness $w = r_{out} - r_{in}$ obtained from PIC simulations for electron density $n_e = 10^{25} \text{ m}^{-3}$ (blue circles). The obtained simulation data can be well fitted by a sum of a logarithmic and a q-Gaussian function from Eq. (4) (solid line).

IV. CNT ARRAY IN 2D AXISYMMETRIC GEOMETRY

Arrays of many coupled nano-channels, e.g. highly-ordered CNT arrays (Fig. 6) or porous alumina, are suitable for channeling wide (transverse micron-scale) beams. It would allow to cover all the transverse beam cross section.

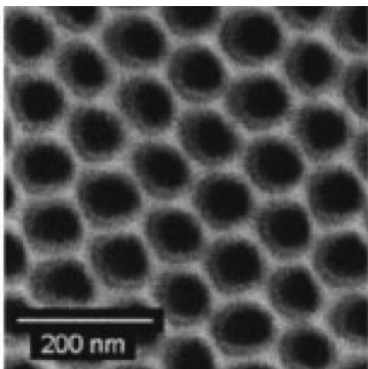


FIG. 6: SEM image of a highly ordered CNT array [58].

The dependence on key parameters, such as the beam density and the tube thickness, is investigated in the

following subsections and compared with analytical estimates.

A. Effective density

Analytical results from the linear theory can be used to describe small-amplitude, laser or beam-driven wakefields in uniform plasmas [9]. Excitation of such wakefields are due to macroscopic, collective effects, caused by the displacement of plasma electrons by the wakefield driver. Hence, under proper conditions, the effect of homogeneous, spatially periodic microscopic departures from uniformity in plasma distribution may be smoothed out in the obtained wakefield. Under such conditions, it might be possible to define an effective density n_{eff} , to be used in the existing analytical expressions, derived for uniform plasmas, to describe wakefields driven in plasmas with small, periodic departures from uniformity. If this is the case, then the effective density can be interpreted as the average density of a unitary plasma cell, i.e., the smallest plasma volume (or surface, if a 2D Cartesian geometry is assumed) which contains a single occurrence of the aforementioned periodic plasma-density pattern. Taking advantage of the 2D axisymmetric geometry adopted for the simulation, the validity of this hypothesis is here verified for a periodic CNT array, composed by multiple concentric cylinders, each of them having the same wall thickness w , separated by gaps with constant width g , as shown in Fig. 7. Such arrangement creates alternating spatial regions, containing either a constant plasma-density n_0 , or vacuum. The longitudinal section of such structure can be seen as a periodic distribution of constant-density plasma layers and gaps. By taking a single unit of this periodic pattern, i.e., one plasma layer, with constant density n_0 and thickness w , and one gap, with “thickness” (width) g , the effective density n_{eff} can be defined as follows:

$$n_{eff} = n_0 / \kappa, \quad \kappa \equiv (w + g)/w. \quad (5)$$

Since the wall and gap thicknesses (w and g , respectively) are non-negative quantities, from Eq. (5) one can see that the upper bound for the effective density is $n_{eff} = n_0$, which is reached for an uniform plasma ($g = 0$, $\kappa = 1$). As gaps are added, the larger the gap with respect to the wall thickness, the lower the effective density. The reciprocal of the coefficient defined in Eq. (5), i.e., $1/\kappa$, can be related to the fraction of the target volume that is filled with constant-density plasma, V_{fill} . For a planar geometry (for example, an array of graphene layers), the relation is straightforward, and $V_{fill} = 1/\kappa$. For a cylindrical geometry (for example, an array of concentric CNTs), the fraction of the filled volume is given by

$$V_{fill}(N, \kappa) = \left[\frac{(N+1)}{N} - \frac{1}{N\kappa} \right] \frac{1}{\kappa}, \quad (6)$$

where $N \equiv r_{out}/(w+g)$ is the number of “repetitions” of the quantity $(w+g)$ within the CNT array maximum ra-

dus, r_{out} . It is worth noting that, for a large number of layers and gaps, $V_{fill} \simeq 1/\kappa$, i.e., Eq. (6) converges to the same expression that describes the fraction of filled volume for a planar geometry. For example, for a large number of evenly distributed plasma layers and gaps ($w = g$), $\kappa = 2$, and $n_{eff} = n_0/2$. Since $1/\kappa = 0.5$, half of the target volume is occupied by plasma with constant-density n_0 , and the other half is empty.

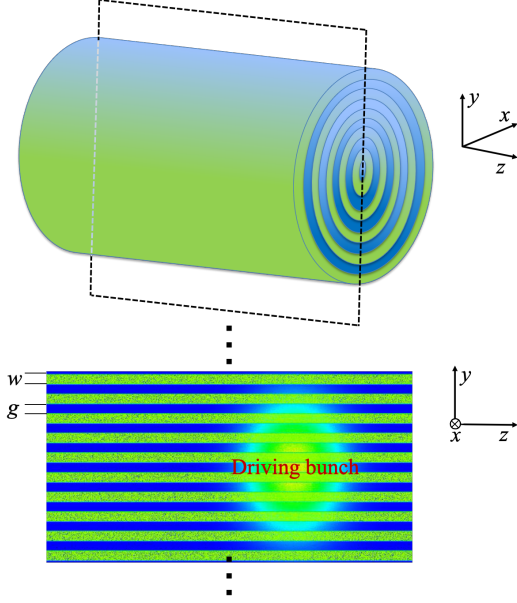


FIG. 7: Schematic of the 2D axisymmetric model of the CNT array.

Existing analytical estimates for wakefields in homogeneous plasmas can be adapted to describe such fields in CNT arrays. This can be achieved by replacing the homogeneous plasma density n_0 in such estimates by the effective density n_{eff} . For example, considering a bi-Gaussian electron beam as the driving source, with density profile given by Eq. (2), from the linear perturbation theory of PWEA, the amplitude of the longitudinal wakefield can be calculated from the following expression [9]:

$$E_z^{max} = \sqrt{\frac{\pi}{2}} E_{0,eff} k_{p,eff}^3 \sigma_\xi \sigma_r^2 \left(\frac{n_b}{n_{eff}} \right) e^{-k_{p,eff}^2 \frac{(\sigma_\xi^2 - \sigma_r^2)}{2}} \times \Gamma(0, k_{p,eff}^2 \sigma_r^2 / 2), \quad (7)$$

where $k_{p,eff} = \omega_{p,eff}/c$ is the plasma wavenumber, calculated using n_{eff} , $E_{0,eff} = m_e c \omega_{p,eff} / e$ is the cold non-relativistic wave breaking field given associated to n_{eff} , and $\Gamma(0, k_{p,eff}^2 \sigma_r^2 / 2)$ the incomplete gamma function.

Figure 8 compares the amplitude of the first accelerating phase of the longitudinal wakefield, E_z^{max} , obtained by means of PIC simulations and analytical estimates from Eq. (7). The wakefield is driven by a bi-Gaussian electron beam propagating in a CNT array. This array has a length of 100 μm , and it is composed by 25

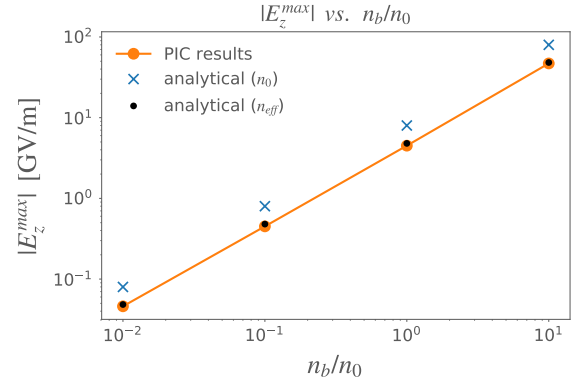


FIG. 8: Numerical and analytical estimates for the amplitude of the longitudinal wakefield E_z^{max} , for distinct values of n_b/n_0 . While estimates obtained assuming n_0 as the plasma density (blue crosses) are overestimated, estimates based on n_{eff} (black dots) show a remarkable agreement with PIC simulation results (orange line).

concentric cylindrical layers, each of them having homogeneous density $n_0 = 10^{19} \text{ cm}^{-3}$ and thickness $w = 40 \text{ nm}$, separated by gaps of equal size (i.e., $g = 40 \text{ nm}$). The first CNT layer has an internal radius of 20 nm. The beam has longitudinal and transverse RMS sizes of $\sigma_\xi = 0.5/k_p \approx 0.84 \mu\text{m}$ and $\sigma_r = 0.1/k_p \approx 0.17 \mu\text{m}$, respectively. The initial beam energy is $E_{k0} = 1 \text{ GeV}$ with an energy spread of $\delta E_{k0}/E_{k0} = 1\%$. The beam charge of each simulation was chosen to provide one of the following values for the normalised peak beam-density, $n_b/n_0 = \{0.01, 0.1, 1, 10\}$. For these values, the beam-driven wakefields will be excited from the linear to the quasi-linear regime. Indeed, despite being derived for small values of n_b/n_0 , the analytical expressions that describe beam-driven wakefields in the linear regime are known to hold reasonably well for $n_b/n_0 \lesssim 10$ [59]. Simulations were performed with a spatial domain of $17 \mu\text{m} \times 2.1 \mu\text{m}$ ($\xi \times r$). Due to the cylindrical symmetry, a single azimuthal mode ($m = 0$) was used, and a grid of 512×318 points ($\xi \times r$) was defined. Moreover, a total density of 36 particles per cell was adopted. It can be seen in Fig. 8 that, while the analytical estimates for E_z^{max} obtained assuming n_0 as the plasma density [9] are overestimated, estimates obtained by using n_{eff} show a remarkable agreement with simulation results, all along the investigated range.

In order to further explore the robustness of analytical estimates based on the effective density, new comparisons are conducted against additional sets of PIC simulations, performed for distinct configurations of CNT arrays. For two distinct wall thicknesses, $w = 20 \text{ nm}$ and 40 nm , respectively, the gap width g is varied in order to obtain values of κ ranging from 1 ($n_{eff} = n_0$) to 3 ($n_{eff} = n_0/3$). A beam charge of $Q \approx 0.6 \text{ pC}$ is set to provide a normalised peak beam-density of $n_b/n_0 = 1$. All the remaining parameters are the same as previously described. Results

of these additional simulations, taken at a propagation distance of $z = 60.5 \mu\text{m}$, can be seen in Fig. 9. As shown in this figure, the analytical estimates of E_z^{max} , obtained for a homogeneous plasma with an effective density n_{eff} , are in agreement with PIC simulation results for a CNT array with a wall thickness of $w = 20 \text{ nm}$. Despite minor departures in the intermediary region of the investigated range of κ values, this agreement holds quite well, even for an effective density as low as $n_{\text{eff}} = n_0/3$. On the other hand, for a CNT array with $w = 40 \text{ nm}$, PIC simulation results show a departure from the analytical estimates of E_z^{max} that increases with κ . This behaviour might be explained as follows. Since the coefficient κ is proportional to the ratio between wall and gap thicknesses, for the same value of κ , a CNT array with thicker walls will have wider gaps as well. While the gaps are thin enough to be “populated” by electrons from its adjacent walls, and while such gaps are small if compared to the beam transverse size, the effective-density model is likely to work fine. However, wide gaps between consecutive CNT-array layers may lead to plasma discontinuities that cannot be smoothed out by the plasma collective effects. Once the interaction between consecutive walls fade, or once the gaps are wide if compared to the beam transverse size, the idea of using an effective density to obtain analytical estimates for the beam-driven wakefield in the CNT array may no longer holds.

From Figs. 10, 11, and 12, PIC simulation results for CNT arrays with a wall thickness of 20 nm and gaps of 5 nm ($\kappa = 1.25$), 20 nm ($\kappa = 2$), and 40 nm ($\kappa = 3$) can be compared against results obtained for their equivalent effective densities, $0.8 n_0$, $0.5 n_0$, and $0.33 n_0$, respectively. In each of these figures, results for the CNT array are shown in the left column (panels a, c, and e), and results for its equivalent effective density are displayed in the right column (panels b, d and f). All results were taken at a propagation distance of $z = 60.5 \mu\text{m}$.

Figure 10(a) depicts the plasma electron density (*purple* color scale), in units of n_0 , for a CNT array with wall thickness of 20 nm and gaps of 5 nm, corresponding to $\kappa = 1.25$. From this panel, one can see the fine layered-structure obtained for these parameters, with a large number of layers and gaps within the beam transverse size. Figure 10(b) shows the same quantity, the plasma electron density, for a homogeneous plasma with an effective density $n_{\text{eff}} = 0.8 n_0$. By comparing panels (a) and (b), one can see that both cases are quantitatively and qualitatively similar. In the same figure, panels (c) and (d) show the longitudinal wakefield E_z , obtained for the CNT array with $\kappa = 1.25$ and for the homogeneous plasma with effective density $n_{\text{eff}} = 0.8 n_0$, respectively. In these panels, the *blue-white-red* color scale represents $E_z(\xi, x, y = 0)$, and the *thick, solid black* line represents the on-axis wakefield outline, $E_z(\xi, x = 0, y = 0)$. In both panels, the *light, dashed black* lines represent the E_z on-axis obtained from the analytical solution, given by Eq. (7), for the adopted effective density ($n_{\text{eff}} = 0.8 n_0$). Both E_z outlines obtained from PIC simulations exhibit a

small departure from the sinusoidal behaviour, observed in the analytical estimates, towards a saw-tooth-like profile. This can be explained by the fact that, for the adopted parameters, the density perturbation observed in panels (a) and (b) resembles a fully-evacuated bubble, which is a characteristic of wakefields driven in the nonlinear regime [9]. The last two panels of Fig. 10 – panels (e) and (f) – show the transverse wakefield $W_\perp \equiv E_r - c B_\theta$. These panels use mostly the same line and color patterns to display quantities analog to those shown in panels (c) and (d), now related to W_\perp rather than to E_z . The only exceptions are the transverse wakefield W_\perp outlines, which are now plotted $0.5 \mu\text{m}$ off-axis, at the position indicated by the *light, dash-dotted* lines in such panels. Since W_\perp is zero on-axis, this was a necessary change. By comparing panels (c) and (e) against panels (d) and (f), respectively, one can see a remarkable agreement between the results obtained for the CNT array and the homogeneous effective density simulations, for both longitudinal and transverse wakefields.

Figure 11 exhibits results for a CNT array with walls and gaps of equal size, $w = g = 20 \text{ nm}$, corresponding to $\kappa = 2$ (left column). With this equality, achieved by setting gaps four-times wider than those of the previous case depicted in Fig. 10, 50% of the the CNT-array volume is empty. Therefore, it is remarkable that the results obtained for the equivalent homogeneous effective density $n_{\text{eff}} = 0.5 n_0$, displayed in the right column of Fig. 11, are still in agreement with the results obtained for the CNT array, shown in the left column of the same figure. With wider gaps, the layered structure in the plasma electron density is more evident in Fig. 11(a). In addition, the horizontal stripes observed in the beam density, alternating regions of higher and lower densities within the gaps and walls, respectively, show how the beam is affected by the CNT layers. Fig. 11(b) shows the electron density for a homogeneous plasma with $n_{\text{eff}} = 0.5 n_0$. Despite the higher peak plasma-electron-density observed in this panel ($\sim 18 n_0$) if compared to panel (a) ($\sim 10 n_0$), the geometry of the electron density perturbation (“bubble” radius and length), as well as the longitudinal and transverse wakefields, are quite similar in both cases. In addition, while the longitudinal wakefield depicted in Fig. 11(c) is smooth and continuous, in Fig. 11(e) a slightly-layered structure in the same color scale shows how the transverse wakefield is affected by the CNT-array gaps.

In Fig. 12, panels (a), (c), and (e) show results for a CNT-array with the same previously adopted wall thickness, $w = 20 \text{ nm}$, and gaps twice as wide as this value, i.e., $g = 40 \text{ nm}$. For this case, $\kappa = 3$, and two thirds of the CNT-array volume are empty. Simulation results for the corresponding homogeneous effective density, $n_{\text{eff}} = 0.33 n_0$, are displayed in panels (b), (d), and (f), in the right column of Fig. 12. Despite the gaps being predominant within the simulation domain, their more pronounced effect in the beam-density distribution and transverse wakefield, and the larger peak

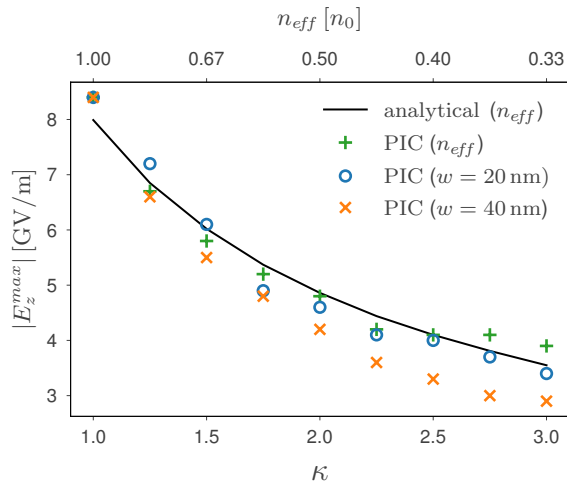


FIG. 9: Numerical and analytical estimates of E_z^{\max} for distinct values of κ . Analytical (black line) and PIC (green crosses) results obtained for a uniform plasma with effective density n_{eff} are in agreement with PIC results for a CNT array with a wall thickness of $w = 20$ nm (blue circles). For $w = 40$ nm (orange cross markers), the agreement decreases as κ is increased.

plasma-electron-density difference between Fig. 12(a) and Fig. 12(b), the results obtained for the equivalent homogeneous effective density are still in agreement with those obtained for the CNT array.

As the beam propagates in a layered structure composed by alternating high and low-density regions, the beam density is periodically modulated by such structure, being lower within the high-density regions due to the strong interference. This effect, which has already been shown by Sahai et al. [36], can be slightly noticed in the aforementioned beam-density modulation depicted in the CNT-array PIC simulation results (left columns of Figs. 10, 11, and 12). In order to observe this modulation in a clearer fashion, Figs. 13(a) and 13(b) display longitudinal and transverse slices of the simulation domain, centered at $y = 0$ and $\xi = 0$ respectively, containing both the beam (transparent-blue-green-yellow color scale) and plasma-electron (purple color scale) densities. In this figure, plotted for a CNT array with $w = g = 20$ nm ($\kappa = 2$) at a propagation distance of $z \simeq 90 \mu\text{m}$, while the lower-half fraction of each panel shows both beam and plasma-electron densities, only the former is depicted in their upper-half region. This configuration allows for a clear view of how the beam density is low/null within the CNT array walls, and high within its gaps. The intensity of this modulation, as well as the rate at which it takes place as the beam propagates along the CNT array, will depend on the beam (initial kinetic energy, density profile) and plasma (density, gap-to-wall ratio) parameters.

V. DISCUSSION AND CONCLUSIONS

Depending on their particular atomic configuration and electrical conduction nature, some solid-state micro- and nanosized structures offer interesting properties to enhance electric field components or induce strong wakefields that could be useful for acceleration, as well as transverse particle guiding and radiation emission. In particular, due to their special optoelectronic, thermal and mechanical properties, 2D materials CNT and graphene based structures might offer novel and alternative solutions to overcome present limitations of standard acceleration techniques.

In this article beam-driven CNT based solid-state plasmonic acceleration has been investigated by means of analytical calculations and numerical PIC simulations, assuming a cold relativistic fluid model, in which the motion of the plasma is not bounded or constrained. As mentioned in Sec. II, this assumption can be a good approximation to describe the collective oscillations of a free electron gas (plasmon) in metallic nanostructures. As indicated in [40, 60] plasmons can be described by the same physics and equations of motion as plasmas.

In CNTs, excited electrons from the conduction band can present mobility on the order of $10^4 \text{ cm}^2/(\text{V}\cdot\text{s})$, practically two orders of magnitude higher than that in metals [61]. Furthermore, following previous studies [39], here we have assumed that the wakefield acceleration of electrons in solid-state plasmas is practically not influenced by ionic lattice effects. Although assuming free mobility of excited plasmon electrons along a CNT based structure might be a reasonable first approximation, in future studies we need to investigate in detail the effects from the movement restrictions imposed by the solid-state properties of the ionic lattice. In the worse case scenario, these restrictions might mitigate the on-axis electron density peaks observed in the PIC simulations presented along this work. As a consequence, the amplitudes of the maximum accelerating fields, E_z^{\max} , which are related to these on-axis density peaks, might be mitigated as well. Therefore, the values here presented must be taken as upper-bound estimates for such amplitudes.

In terms of the ionic lattice, another question is the survivability of the solid-state sample interacting with the wakefield driver (a relativistic particle beam in our case). The lattice will be highly ionized by the driver and, to be effective, the accelerating wakefield must precede any lattice dissociation due to the ion motion. According to [62, 63] an ionic crystalline solid dissociates by absorbing plasmon energy on a timescale determined by $\Delta t \approx \sqrt{m_i/m_e}(2\pi/\omega_p)$, where m_i and m_e are the rest mass of the ion and the electron respectively. It depends on the plasma frequency ω_p . Assuming plasma densities $n_0 \approx 10^{25} \text{ m}^{-3}$, we obtain a lattice dissociation time $\Delta t \sim 1$ ps. As we have shown in the results of previ-

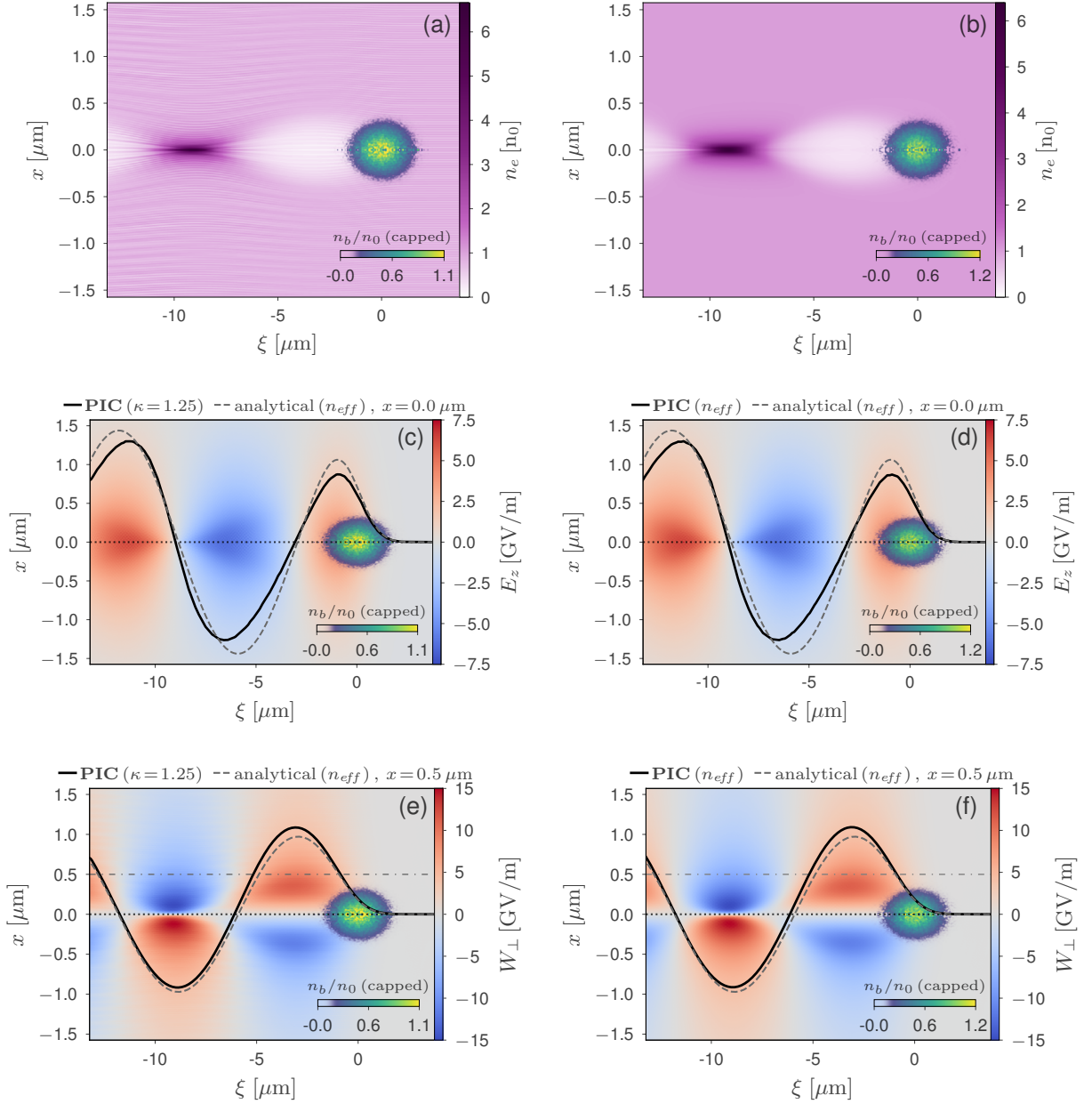


FIG. 10: Simulation results for a CNT array with $w = 20$ nm and $g = 5$ nm ($\kappa = 1.25$, *left column*), compared to simulation results for an homogeneous plasma, with $n_{eff} = 0.8 n_0$ (*right column*), at a propagation distance of $z = 60 \mu\text{m}$. Panels (a) and (b) show the normalised plasma electron density (*purple* color scale), panels (c) and (d) depict the longitudinal wakefields, and panels (e) and (f) illustrate the transverse wakefields. The fields obtained from PIC simulation results are shown as *blue-grey-red* colored regions, with *thick, solid black* lines representing the on-axis ($x = 0$) outline of the longitudinal wakefields, and the off-axis ($x = 0.5 \mu\text{m}$) outline of the transverse wakefields. Outlines for these same fields, obtained from effective-density-based analytical estimates (*light, dashed black* lines), are provided as well. All panels show the beam density distribution (*transparent-blue-green-yellow* color scale), capped (saturated) to emphasize internal perturbations caused by the CNT array layers.

ous sections, in the wakefield excitation we are dealing with timescales < 100 fs. Therefore, the wakefield may build-up before the lattice dissociates.

In this article, the wakefield excitation in CNT based hollow solid-state structures has been studied by means

of 2D axisymmetric PIC simulations using the code FBPIC [38]. Different system configurations have been studied. First, we have investigated the case of a single tube which is basically a hollow plasma channel with a micrometric inner aperture. The channel walls are as-

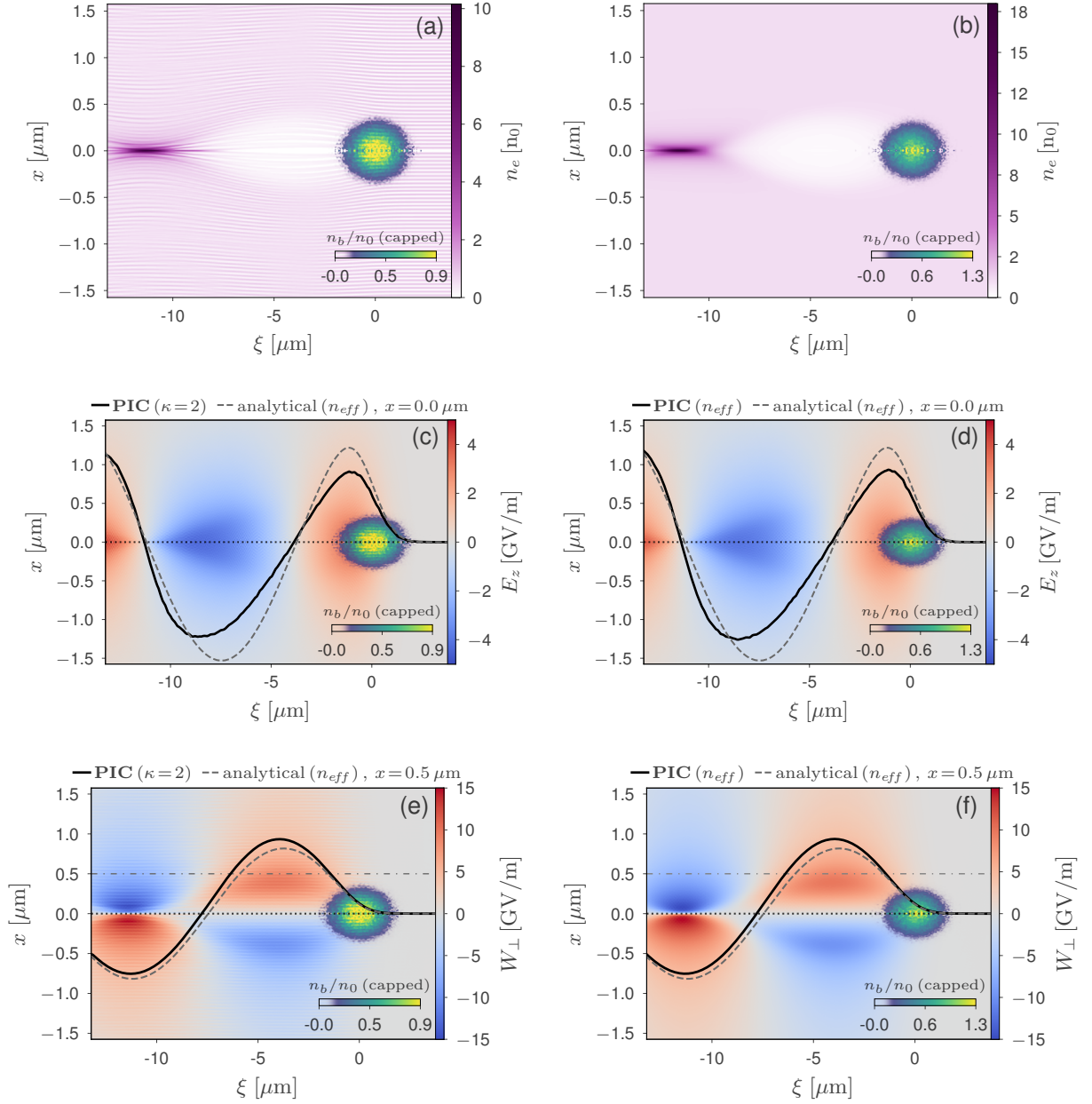


FIG. 11: Simulation results for a CNT array with $w = 20$ nm and $g = 20$ nm ($\kappa = 2$, *left column*), compared to simulation results for an homogeneous plasma, with $n_{\text{eff}} = 0.5 n_0$ (*right column*), at a propagation distance of $z = 60$ μm . Panels (a) and (b) show the normalised plasma electron density (*purple* color scale), panels (c) and (d) depict the longitudinal wakefields, and panels (e) and (f) illustrate the transverse wakefields. The fields obtained from PIC simulation results are shown as *blue-grey-red* colored regions, with *thick, solid black* lines representing the on-axis ($x = 0$) outline of the longitudinal wakefields, and the off-axis ($x = 0.5$ μm) outline of the transverse wakefields. Outlines for these same fields, obtained from effective-density-based analytical estimates (*light, dashed black* lines), are provided as well. All panels show the beam density distribution (*transparent-blue-green-yellow* color scale), capped (saturated) to emphasize internal perturbations caused by the CNT array layers.

sumed to be formed of CNT bundles that will act as a solid-state plasma under the excitation and ionization driven by an external beam crossing the channel. A systematic parameter scan has been performed to study the dependence of the maximum longitudinal electric field

E_z^{max} on the tube aperture and wall thickness. This has allowed us to obtain analytical expressions for E_z^{max} to make quick predictions.

In the second part of this paper, a CNT array has been modeled in a 2D axisymmetric geometry. For the sake of

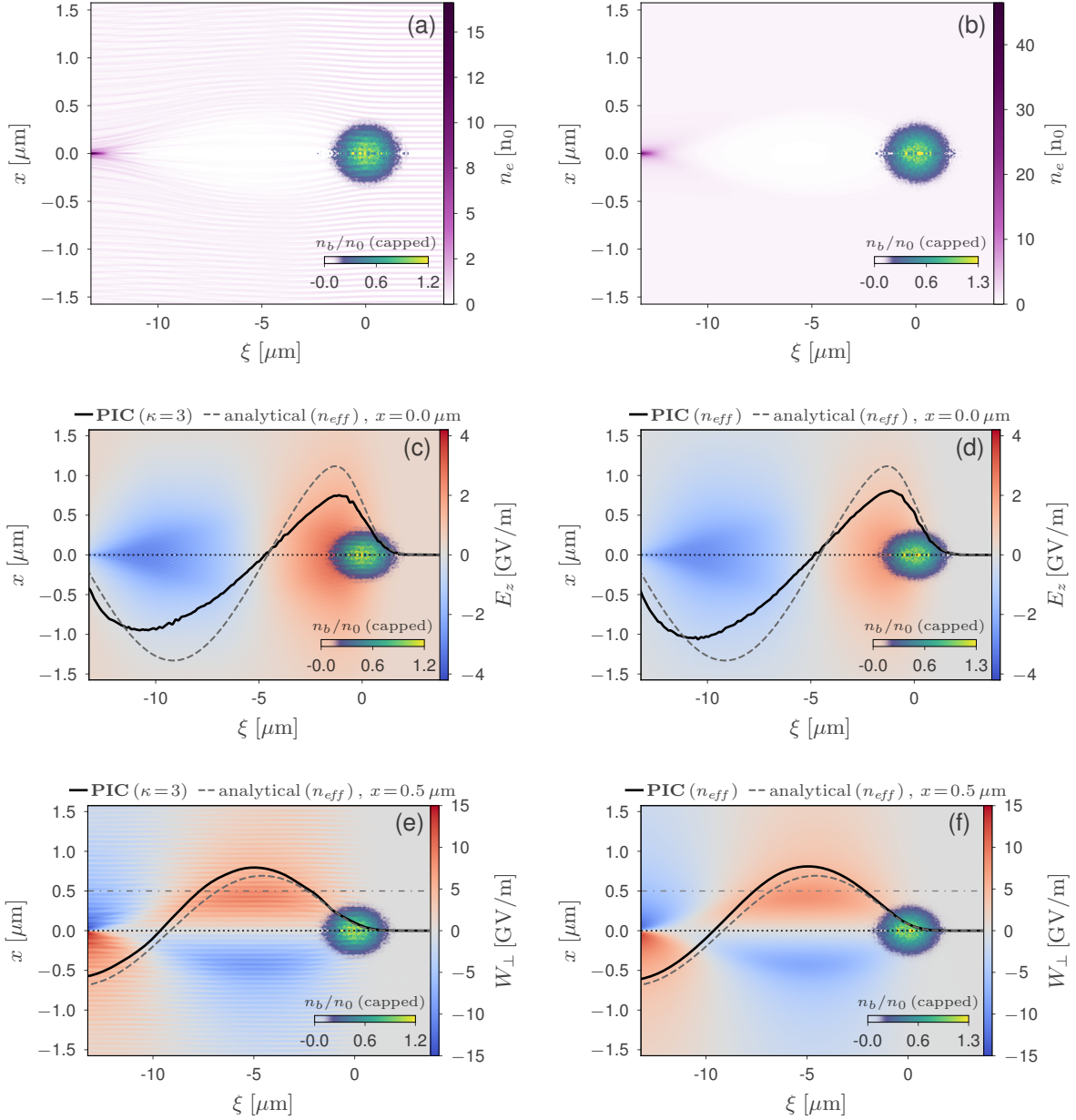


FIG. 12: Simulation results for a CNT array with $w = 20$ nm and $g = 40$ nm ($\kappa = 3$, *left column*), compared to simulation results for an homogeneous plasma, with $n_{eff} = 0.33 n_0$ (*right column*), at a propagation distance of $z = 60 \mu\text{m}$. Panels (a) and (b) show the normalised plasma electron density (*purple* color scale), panels (c) and (d) depict the longitudinal wakefields, and panels (e) and (f) illustrate the transverse wakefields. The fields obtained from PIC simulation results are shown as *blue-grey-red* colored regions, with *thick, solid black* lines representing the on-axis ($x = 0$) outline of the longitudinal wakefields, and the off-axis ($x = 0.5 \mu\text{m}$) outline of the transverse wakefields. Outlines for these same fields, obtained from effective-density-based analytical estimates (*light, dashed black* lines), are provided as well. All panels show the beam density distribution (*transparent-blue-green-yellow* color scale), capped (saturated) to emphasize internal perturbations caused by the CNT array layers.

comparison, it is worth mentioning that previously similar studies were performed considering a 2D Cartesian symmetry using the PIC code EPOCH [21]. Due to its 2D Cartesian geometry, the system simulated in Ref. [21] is closer to a multilayer nanostructure alternating straight

plasma layers and empty space. It could represent either multilayer graphene structures or a sequence of thick layers made of CNT bundles. Assuming similar parameters, in comparison to 2D Cartesian, the wakefield amplitudes obtained from 2D axisymmetric simulations are approx-

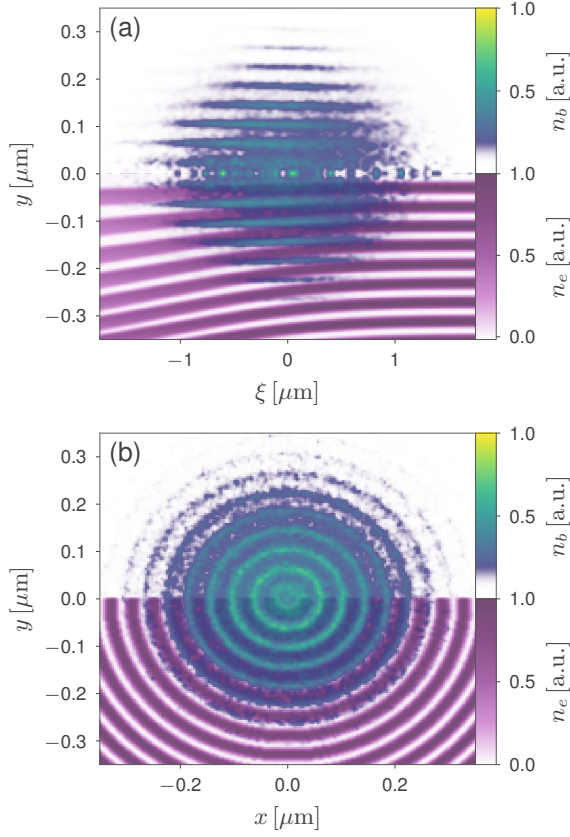


FIG. 13: (a) Longitudinal and (b) transverse sections showing both the plasma electron and beam densities, n_e and n_b , respectively, plotted in arbitrary units (a.u.) at a propagation distance of $z = 92.5 \mu\text{m}$. While both densities are shown in the lower-half region of each panel, only n_b is displayed in their upper-half region.

imately one order of magnitude lower, matching analytical estimates from the linear theory while in the linear regime (see Fig. 8).

The adoption of an effective density n_{eff} allows existing analytical estimates, derived for wakefields excited in homogeneous plasmas in the linear regime, to be used for describing wakefields excited in CNT arrays. The accuracy of this approach for estimating the amplitude of the longitudinal wakefield accelerating amplitude E_z^{max} was verified as follows. PIC simulations for homogeneous plasmas with effective densities given by $n_{\text{eff}} = n_0/\kappa$ were performed for values of κ ranging from $\kappa = 1$, representing a uniform plasma with no gaps, to $\kappa = 3$, representing CNT arrays with gaps three times wider than the CNT wall thicknesses. The accelerating field amplitudes E_z^{max} obtained from such simulations show good agreement with the aforementioned analytical estimates (Fig. 9). Two additional sets of PIC simulations were performed, each of them assuming CNT arrays with wall thicknesses of 20 nm and 40 nm, respectively, with κ varying from 1 to 3. From the PIC simulation results for

the 20-nm CNT arrays, it can be seen that E_z^{max} shows good agreement with the analytical estimates obtained by using the effective density n_{eff} , all along the range of investigated κ values. On the other hand, results for the 40-nm CNT show that this agreement is reduced as the gaps get wider with respect to the CNT wall thickness.

It is worth noting that, as the gaps (and, consequently, κ) are increased, the wavelength of the wakefield driven in the CNT array decreases accordingly with the plasma wavelength associated to the effective density n_{eff} . In other words, the wakefield wavelength scales with an effective plasma wavelength, $\lambda_{p,\text{eff}} = 2\pi/k_{p,\text{eff}}$. This finding may be relevant for obtaining analytical estimates for plasma-based suitable parameters for the wakefield driver, as well as limiting parameters such as the length of the accelerating/decelerating wakefield phase, or the dephasing and depletion lengths if a laser pulse is adopted as the wakefield driver.

Analytical estimates obtained by using the effective density may provide upper-bound estimates for the accelerating fields in plasmas with complex, periodic profiles. The accuracy of such estimates obtained by using this approach might depend on how large is an unitary cell of plasma periodic pattern, if compared to the beam driver size. For the largest departure from an homogeneous plasma presented in this paper, i.e., for $\kappa = 3$ ($n_{\text{eff}} = 0.33 n_0$), the size of such an unitary cell is approximately $0.07 \sigma_r$ and $0.14 \sigma_r$ for the 20-nm and 40-nm CNT arrays, respectively. The accuracy of the effective density approach might be affected by the CNT-wall plasma density as well. While very low densities might not have enough electrons to populate the gaps, higher densities may decrease the transverse reach of the wakefield, which scales with k_p^{-1} . In a future work, further investigation will be conducted on the validity and limitations of the effective density approach. Future studies will also include the design of possible experiments to validate some of the aspects of results described in this article.

Eventually, nanostructured materials based on CNTs and graphene could lead to novel pathways to access multi-GV/m and multi-TV/m field regimes towards more sustainable, compact and low-cost accelerating methods. This could open new horizons to the physics of extreme fields, particularly in collider physics, light sources, and in many other areas of applied sciences, medicine and industry.

ACKNOWLEDGMENTS

This project is supported by the Generalitat Valenciana (CIDEAGENT/2019/058). The authors acknowledge computing resources provided by STFC's SCARF cluster, the University of Manchester's CSF3 cluster, and the CNPq (Chamada Universal 427273/2016-1). Finally, the authors thank the FBPIC and OpenPMD developers, for their contributions to the scientific community, and Aakash Sahai, for his previous collaboration with our group.

-
- [1] T. Abe, et al., “Breakdown study based on direct in situ observation of inner surfaces of a rf accelerating cavity during a high-gradient test”, *Phys. Rev. Accel. Beams* **19**, 102001 (2016).
 - [2] J. Breuer and P. Hommelhoff, “Laser-Based Acceleration of Nonrelativistic Electrons at a Dielectric Structure”, *Phys. Rev. Lett.* **111**, 134803 (2013).
 - [3] E. A. Peralta, et al., “Demonstration of electron acceleration in a laser-driven dielectric microstructure”, *Nature* **503**, 91 (2014).
 - [4] R. J. England, R. J. Noble, eds., “Dielectric laser accelerators”, *Reviews of Modern Physics* **86**, 1337 (2014).
 - [5] T. Tajima and J. Dawson, “Laser Electron Accelerator”, *Phys. Rev. Lett.* **43** (4), 267 (1979).
 - [6] P. Chen, et al., “Acceleration of Electrons by the Interaction of a Bunched Electron Beam with a Plasma”, *Phys. Rev. Lett.* **54** (7), 693 (1985).
 - [7] W. P. Leemans, et al., “GeV electron beams from a centimetre-scale accelerator”, *Nature Physics* **2**, 696 (2006).
 - [8] M. Litos, et al., “High-efficiency acceleration of an electron beam in a plasma wakefield accelerator”, *Nature* **515** (7525), 92 (2014).
 - [9] E. Esarey, C. Schroeder, and W.P. Leemans, “Physics of laser-driven plasma-based electron accelerators”, *Reviews of Modern Physics*, 81(3), 1229–1285 (2009).
 - [10] T. Tajima and M. Cavenago, “Crystal X-ray accelerator”, *Phys. Rev. Lett.* **59**, 1440 (1987).
 - [11] P. Chen and R. J. Noble, “Crystal channel collider: Ultra-high energy and luminosity in the next century”, *AIP Conf. Proc.* **398**, 273 (1997) and references therein.
 - [12] G. Mourou, et al., “Single cycle thin film compressor opening the door to Zeptosecond-Exawatt physics”, *Eur. Phys. J. Spec. Top.* **223**, 1181 (2014).
 - [13] X. Zhang, et al., “Particle-in-cell simulation of X-ray wakefield acceleration and betatron radiation in nanotubes”, *Phys. Rev. Spec. Top. Accel. Beams* **19**, 101004 (2016).
 - [14] Ping Li, et al., “Recent advances in focused ion beam nanofabrication for nanostructures and devices: fundamentals and applications”, *Nanoscale* **13**, 1529 (2021).
 - [15] Cary L. Pint, et al., “Dry Contact Transfer Printing of Aligned Carbon Nanotube Patterns and Characterization of Their Optical Properties for Diameter Distribution and Alignment”, *ACS Nano* **4**, 1131 (2010).
 - [16] X. Chen, et al., “Atomic layer lithography of wafer-scale nanogap arrays for extreme confinement of electromagnetic waves”, *Nat. Commun.* **4**, 2361 (2013).
 - [17] Andrea Pizzi, et al., “Graphene Metamaterials for Intense, Tunable, and Compact Extreme Ultraviolet and X-Ray Sources”, *Adv. Sci.* **7**, 1901609 (2020).
 - [18] Ling-Bao Kong and Zhaoyang Chen, “Plasmonic electron acceleration with meta-surfaces”, *Phys. Plasmas* **24**, 083111 (2017).
 - [19] Y. M. Shin, D. A. Still and V. Shiltsev, “X-ray driven channelling acceleration in crystals and carbon nanotubes”, *Phys. Plasmas* **20**, 123106 (2013).
 - [20] Y. M. Shin, et al., “Ultra-High Gradient Beam-Driven Channeling Acceleration in Hollow Crystalline Media”, *Proc. of IPAC’14*, paper TUPME061, Dresden, Germany, June 2014.
 - [21] J. Resta-Lopez, et al., “Study of Ultra-High Gradient Acceleration in Carbon Nanotube Arrays”, *Proc. of IPAC’18*, paper TUXGBE2, Vancouver, Canada, Apr.-May 2018.
 - [22] D. Sarid, W. Challener, “Modern Introduction to Surface Plasmons: Theory, Mathematica Modeling, and Applications”, Cambridge University Press, 2010. 371 p. DOI: 10.1017/CBO9781139194846.
 - [23] M. Shoufie Ukhtary and Riichiro Saito, “Surface plasmon in graphene and carbon nanotubes”, *Carbon* **167**, 455 (2020).
 - [24] A. Macchi, “Surface plasmons in superintense laser-solid interactions”, *Phys. Plasmas* **25**, 031906 (2018).
 - [25] L. Fedeli, et al., “Electron Acceleration by Relativistic Surface Plasmons in Laser-Grating Interactions”, *Phys. Rev. Lett.* **116**, 015001 (2016).
 - [26] William Que, “Theory of plasmons in carbon nanotube bundles”, *J. Physics: Condens. Matter* **14**, 5239 (2002).
 - [27] M. Nejati, et al., “The single-wall carbon nanotube waveguides and excitation of their $\sigma + \pi$ plasmons by an electron beam”, *Phys. Plasmas* **16**, 022108 (2009).
 - [28] T. Stöckli, et al., “Collective oscillations in a single-wall carbon nanotube excited by fast electrons”, *Phys. Rev. B* **64**, 032901 (2001).
 - [29] Y-N. Wang and Z. L. Miskovic, “Interactions of fast ions with carbon nanotubes: Self-energy and stopping power”, *Phys. Rev. A* **69**, 022901 (2004).
 - [30] D. J. Mowbray, et al., “Wake effect in interactions of fast ions with carbon nanotubes”, *Phys. Lett. A* **329**, 94 (2004).
 - [31] Y. M. Shin, “Optically controlled coherent X-ray radiations from photo-excited nanotubes”, *Nucl. Instrum. Meth. Phys. Res. B* **407**, 276 (2017).
 - [32] D. Strickland, G. Mourou, “Compression of amplified chirped optical pulses”, *Optics Communications* **56**(3), 219 (1985).
 - [33] V. Yakimenko et al., “FACET-II facility for advanced accelerator experimental tests”, *Phys. Rev. Acc. Beams* **22**, 101301 (2019).
 - [34] A. A. Sahai, “Excitation of a nonlinear plasma ion wake by intense energy sources with applications to the crunch-in regime”, *Phys. Rev. Accel. Beams* **20**, 081004 (2017).
 - [35] A. A. Sahai, T. Tajima, P. Taborek, and V.D. Shiltsev, “Solid-state tube wakefield accelerator using surface waves in crystals”, *International Journal of Modern Physics A*, **34**, 1943009–29 (2020).
 - [36] A. A. Sahai, “Nanomaterials Based Nanoplasmonic Accelerators and Light-Sources Driven by Particle-Beams”, *IEEE Access* **9**, 54831 (2021).
 - [37] A. A. Sahai, et al., “Plasmonic accelerators for colliders with PetaVolts per meter gradients”, *Proc. of the US Community Study on the Future of Particle Physics (Snowmass 2021)*; arXiv:2203.11623 [physics.acc-ph], 2022.
 - [38] R. Lehe, M. Kirchen, I.A. Andriyash, B.B. Godfrey, and J.-L. Vay, “A spectral, quasi-cylindrical and dispersion-free Particle-In-Cell algorithm”, *Computer Physics Communications*, **203**, 66–82 (2016).
 - [39] S. Hakimi, et al., “Wakefield in solid state plasma with the ionic lattice force”, *Physics of Plasmas*, **25**(2), 023112 (2018)

- [40] W.J. Ding, et al., “Particle simulation of plasmons”, *Nanophotonics*, **9**(10), 3303–3313 (2020).
- [41] G.K. Ngirmang, et al., “Three dimensional particle-in-cell simulations of electron beams created via reflection of intense laser light from a water target”, *Phys. Plasmas* **23**, 043111 (2016).
- [42] A. Lifschitz, et al., “Particle-in-Cell modelling of laser–plasma interaction using Fourier decomposition”, *Journal of Computational Physics*, **228**(5), 1803–1814 (2009).
- [43] B.B. Godfrey, “Numerical Cherenkov instabilities in electromagnetic particle codes”, *Journal of Computational Physics*, **15**(4), 504–521, (1974).
- [44] F. Albert et al., “2020 roadmap on plasma accelerators”, *New J. Phys.* **23**, 031101 (2021).
- [45] C. Zhu, Z. Xie, K. Guo, “Formation of close-packed multi-wall carbon nanotube bundles”, *Diamond and Related Materials* **13**(1), 180 (2004).
- [46] G. Lalwani, et al., “Fabrication and Characterization of Three-Dimensional Macroscopic All-Carbon Scaffolds”, *Carbon* **53**, 90 (2012).
- [47] C. M. Lange, T.-C. Shen, “Fabrication of height-modulated carbon nanotube forest: Morphologies and prospects for broad band absorption”, *Carbon Trends* **4**, 100070 (2021).
- [48] P. Chen and R. J. Noble, “A solid state accelerator” *AIP Conf. Proc.* **156**, 222 (1987)
- [49] D. Östling, D. Tománek, and A. Rosén, “Electronic structure of single-wall, multiwall, and filled carbon nanotubes”, *Phys. Rev. B*, **55**(20), 13980–13988 (1997)
- [50] A. Marocchino, et al., “Experimental characterization of the effects induced by passive plasma lens on high brightness electron bunches”, *Appl. Phys. Lett.* **111**, 184101 (2017).
- [51] H. Nakanishi, et al., “Direct Observation of Plasma-Lens Effect”, *Phys. Rev. Lett.* **66**, 1870 (1991).
- [52] T.C. Chiou, et al., “Laser wake-field acceleration and optical guiding in a hollow plasma channel”, *Physics of Plasmas*, **2**(1), 310–318 (1995).
- [53] T.C. Chiou, and T. Katsouleas, “High Beam Quality and Efficiency in Plasma-Based Accelerators”, *Phys. Rev. Lett.*, **81**(16), 3411–3414 (1998).
- [54] C.B. Schroeder, D.H. Whittum, and J.S. Wurtele, “Multimode Analysis of the Hollow Plasma Channel Wakefield Accelerator”, *Phys. Rev. Lett.*, **82**(6), 1177–1180 (1999).
- [55] W.D. Kimura, et al., “Hollow plasma channel for positron plasma wakefield acceleration”, *Phys. Rev. ST Accel. Beams*, **14**(4), 969–11 (2011).
- [56] E. Adli, et al., “Demonstration of a positron beam-driven hollow channel plasma wakefield accelerator”, *Nature Communications*, **7**(1), 1–6 (2016).
- [57] Y. Li, et al., “High-quality electron beam generation in a proton-driven hollow plasma wakefield accelerator”, *Phys. Rev. Accel. Beams* **20**, 101301 (2017).
- [58] H. Gao, et al., “Field emission of large-area and graphitized carbon nanotube array on anodic aluminium oxide template”, *Journal of Applied Physics* **93** (9), 5602 (2003).
- [59] W. Lu, C. Huang, M.M. Zhou, W.B. Mori, and T. Katsouleas, “Limits of linear plasma wakefield theory for electron or positron beams”, *Physics of Plasmas* **12**(6), 063101 (2005).
- [60] A. E. Rider, K. Ostrikov, and S. A. Furman, “Plasmas meet plasmonics: Everything old is new again”, *Eur. Phys. J. D* **66**, 226 (2012).
- [61] S. Hong, S. A. Myung, “Flexible approach to mobility”, *Nat. Nanotechnol.* **2**, 207 (2007).
- [62] P. Chen, R. J. Noble, “Crystal Channel Collider Ultra-High Energy and Luminosity in the Next Century”, *SLAC-PUB-7402*, April 1998.
- [63] Y. M. Shin, A. Lumpkin, R. M. Thurman-Keup, V. Shiltsev, “Feasibility of Continuously Focused TeV/m Channeling Acceleration with CNT-Channel”, *Proc. of IPAC2015, WEPWA072*, Richmond, VA, USA, 2015.